Terahertz-driven irreversible topological phase transition in two-dimensional $MoTe_2$

Jiaojian Shi[1†], Ya-Qing Bie[2,5*†], Wei Chen[3], Shiang Fang[3], Jinchi Han[4], Zhaolong Cao[5], Takashi Taniguchi[6], Kenji Watanabe[6], Vladimir Bulović[4], Efthimios Kaxiras[3], Pablo Jarillo-Herrero[2*], Keith A. Nelson[1*].

[1]Department of Chemistry, Massachusetts Institute of Technology, Cambridge, MA 02139, USA

[2]Department of Physics, Massachusetts Institute of Technology, Cambridge, MA 02139, USA

[3]Department of Physics, Harvard University, Cambridge, MA 02138, USA

[4]Department of Electrical Engineering and Computer Science, Massachusetts Institute of Technology, Cambridge, MA 02139, USA

[5]State Key Lab of Optoelectronic Materials and Technologies, Guangdong Province Key Laboratory of Display Material and Technology, School of Electronics and Information Technology, Sun Yat-sen University, Guangzhou, 510275, People's Republic of China

[6]Advanced Material Laboratory, National Institute of Material Science, Tsukuba, Ibaraki 305-0044, Japan

[†]These authors contributed equally to this work

[*]Corresponding author: kanelson@mit.edu pjarillo@mit.edu bieyq@mail.sysu.edu.cn

Abstract:

Recent discoveries of broad classes of quantum materials have spurred fundamental study of what quantum phases can be reached and stabilized, and have suggested intriguing practical applications based on control over transitions between quantum phases with different electrical, magnetic, and/or optical properties. Tabletop generation of strong terahertz (THz) light fields has set the stage for dramatic advances in our ability to drive quantum materials into novel states that do not exist as equilibrium phases[1-4]. However, THz-driven irreversible phase transitions are still unexplored. Large and doping-tunable energy barriers between multiple phases in two-dimensional transition metal dichalcogenides (2D TMDs) provide a testbed for THz polymorph engineering[5,6]. Here we report experimental demonstration of an irreversible phase transition in 2D $MoTe_2$ from a semiconducting hexagonal phase (2H) to a predicted topological insulator distorted octahedral (1T′) phase[7] induced by field-enhanced terahertz pulses. This is achieved by THz field-induced carrier liberation and multiplication processes that result in a transient high carrier density that favors the 1T′ phase. Single-shot time-resolved second harmonic generation (SHG) measurements following THz excitation reveal that the transition out of the 2H phase occurs within 10 ns. This observation opens up new possibilities of THz-based phase patterning and has implications for ultrafast THz control over quantum phases in two-dimensional materials.

Quantum materials with topological order are now at the forefront of condensed matter science because they cannot be described by the classical Fermi liquid theory[8] and have topological properties that could lead to high-performance electronics and fault-tolerant quantum computing[9,10]. Because of their wide ranges of chemical compositions and crystal structures, two-dimensional transition metal dichalcogenides (2D TMDs) have multiple quantum phases[5] and can provide an excellent platform for observation of transitions among them[5,6,11-17], including 2D phase transitions between topologically trivial and non-trivial states. The distorted octahedral (1T′) phase in several types of 2D TMDs, including 2D $MoTe_2$, is unique as it is predicted to exhibit a nontrivial topological edge state[7]. The energy difference between hexagonal (2H) and distorted octahedral (1T′) structures in 2D $MoTe_2$ is substantially smaller than the energy differences in other 2D TMDs[18]. However, control over the phase transition is difficult because of the large energy barrier that separates the two phases at room temperature[7]. Carrier injection[6] using ionic liquid gating leads to a 2H-1T′ phase transition in monolayer $MoTe_2$, but the phase transition is reversed once the gate is turned off. An irreversible phase transition in bulk $MoTe_2$ induced by visible laser irradiation[19] was reported, but follow-up Raman measurements and theoretical calculations indicate that the new phase is a compositionally altered Te-metalloid-like phase rather than the 1T′ phase[18,20,21]. Here we report the use of THz-frequency pulses to induce an irreversible 2H-1T′ phase transition in monolayer and bilayer $MoTe_2$.

A strong THz-frequency electric field can generate high carrier densities through Poole-Frenkel ionization or similar mechanisms that liberate carriers, and can accelerate the liberated or pre-existing carriers to multi-eV energies sufficient for impact ionization that liberates even more carriers that can be accelerated to continue a cascading process[22]. This approach has been used to drive the correlated electron system VO_2 from its insulating phase into a transient conducting

phase[1,23], though the transition is reversed upon electronic and thermal relaxation. Theoretical calculations show that a high carrier density can invert the energy ordering of 2H and 1T′ phases in $MoTe_2$ and lower the energy barrier between them, which can enable a rapid and possibly irreversible phase transition[24-26]. However, it may be challenging to generate a sufficiently strong free-space THz field with tabletop THz techniques[27].

In our experiment, ~ 0.3 MV/cm free-space THz fields were used[27] and were further strengthened with simple field enhancement structures (FES) consisting of 100 μm-wide parallel gold strips deposited onto fused silica substrates, separated by 1.8 μm capacitive gaps. **Figure 1a** illustrates that a single-layer $MoTe_2$ flake encapsulated with top and bottom hexagonal boron nitride (h-BN) layers was placed carefully on top of a gap between gold lines. A THz field polarized perpendicular to the gold lines is enhanced up to 2 orders of magnitude in the capacitive gaps[28] according to finite-difference time-domain calculations, as shown in **Fig.1b**. **Figure 1c** shows an optical image of a typical sample prepared using a dry transfer method[29] under a microscope. The h-BN layers can isolate $MoTe_2$ from possible field-induced charge emission from the gold layers[30] and avoid degradation of the 1T′ phase in air. We used Raman spectroscopy to observe changes in the lattice vibrational spectrum following THz irradiation. As in earlier Raman spectroscopy of 2H-$MoTe_2$ monolayers and bilayers[31], we used an excitation wavelength of 633 nm from a He-Ne laser and kept the power below 1 $\mathrm{mW}/\mu\mathrm{m}^2$ to avoid optically induced sample damage[19]. As indicated in **Fig. 1d**, before THz irradiation, monolayer 2H-$MoTe_2$ within the gap shows two characteristic Raman peaks at 171.5 cm^{-1} (out-of-plane A_{1g} mode) and 236 cm^{-1} (in-plane E_{2g} mode) with the relative intensity in agreement with earlier observations[18]. After irradiation with five THz pulses whose field strength in free space was 270 kV/cm (here and below, we report the field strengths prior to field enhancement at the samples), the A_{1g} and E_{2g} peaks of 2H monolayer $MoTe_2$ almost

disappear and a new peak appears at 163.3 cm^{-1}, which agrees very well with the theoretically calculated frequency of 163 cm^{-1} for the A_g mode of the monolayer 1T′-$MoTe_2$ phase[18]. We do not see peaks near 122 cm^{-1} or 141 cm^{-1} which are assigned to Te-metalloid-like modes[21]. The new peak at 163.3 cm^{-1} is strengthened upon further irradiation and the Raman spectra are consistent with a THz-induced 2H-to-1T′ phase transition in $MoTe_2$.

The THz field-dependence of the $MoTe_2$ response was examined by irradiating a sample with a succession of eleven THz pulses with gradually increasing free-space field strength up to a maximum of 270 kV/cm. We used optical second harmonic generation (SHG) to monitor change in the crystal symmetry, from non-centrosymmetric in the 2H phase to centrosymmetric in the 1T′ phase. After each THz pulse, an image of the SHG intensity from the crystal was recorded. Three images (prior to irradiation and following THz fields with free-space amplitudes of 183 kV/cm and 240 kV/cm) are shown in **Fig. 2a**, and supplementary Fig. S6 shows the complete set of images recorded after THz pulses with field strengths successively incremented by ~ 20-30 kV/cm. A plot of the SHG intensities measured at three sample locations within the field-enhancement gap (labeled A, B, C in **Fig. 2a**) is presented in **Fig. 2b**. (See **Methods** section and Supplementary Fig. S5 for experimental details.) The first clearly observable drop in SHG signal occurred upon irradiation with one THz pulse whose field strength was 183 kV/cm. The SHG intensity dropped precipitously after one pulse with a free-space field amplitude of 240 kV/cm and essentially disappeared after a final pulse with 270 kV/cm amplitude. The field enhancement factor in these three regions is approximately 20, so the threshold for a measurable drop in SHG intensity is approximately 4.0 MV/cm. Raman spectra were also measured after irradiation with increasing field strengths. **Figure. 2c** shows spectra after irradiation with field strengths of 200 kV/cm and 270 kV/cm. As in the SHG results, the first clear drop in strengths of the 2H phase Raman lines

occurs upon irradiation with one pulse with about 200 kV/cm amplitude, and the lines almost disappear completely after a single 270 kV/cm pulse. The 1T′ phase Raman line grows in and dominates the spectrum after irradiation with 1000 pulses at 270 kV/cm.

Figure 2d shows field-dependent Raman spectra from an h-BN-encapsulated bilayer $MoTe_2$ sample before and after THz irradiation. The bilayer $MoTe_2$ within the gap initially shows characteristic Raman peaks at 171.5 cm^{-1} (A_{1g}) and 236 cm^{-1} (E_{2g}) as in the monolayer, and also a B_{2g} peak (out-of-plane interlayer mode) at 291 cm^{-1}, with relative peak intensities consistent with earlier results[31,32]. As in the monolayer, no obvious changes were observed when the THz field strength was below 200 kV/cm. We see a reduction in A_{1g} and E_{2g} Raman lines after a single THz pulse at 200 kV/cm. After irradiating with THz pulses at 270 kV/cm, a new peak appears at 163.2 cm^{-1}, which is consistent with the theoretically calculated value for the A_g mode of a pristine 1T′ phase bilayer $MoTe_2$[18]. (An expanded view of the Raman line and a fit to it are shown in Supplementary Fig. S4). The bilayer sample region examined by the Raman laser spot shows a mixture of 2H and 1T′ phases after irradiation with 1000 pulses at 270 kV/cm.

Our static Raman and SHG measurements clearly indicate that a new crystalline phase is induced by the enhanced THz field. We repeated SHG and Raman spectroscopy measurements like those described above on two additional monolayer samples with essentially identical results, which are presented in the Supplementary Fig. S2. Each sample was permanently altered after THz high-field measurements were carried out. We checked to see that samples did not return to the 2H phase even weeks after strong-field irradiation.

To gain mechanistic insight into the THz-driven phase transition, direct time-resolved observation of the far-from-equilibrium dynamics is crucial. However, the irreversible nature of the phase transition precludes conventional ultrafast spectroscopy in which both excitation and probe pulses

perturb and interrogate the sample many times with different pump-probe delay times, with the sample fully recovering to its initial state between measurements. We conducted THz-pump SHG-probe measurements using a fresh sample for each single-shot measurement, with the THz pump field exceeding the phase transition threshold. Each measurement yielded data at only one probe delay time. (See Supplementary Note 3 and Fig. S7 for experimental details.) SHG signals from monolayer samples were too weak to measure on a single-shot basis, even with an incident 800-nm pulse fluence well above the optical damage threshold, which is quite low[19] for 2D $MoTe_2$. (The static SHG measurements discussed above were conducted by signal-averaging over many pulses at low fluence.) Stronger SHG signals can be generated from several-layer samples[33], and we obtained measurable single-shot signals from trilayer samples using a pulse fluence of ~ 20 mJ/cm^2. Trilayer samples used here were not encapsulated with h-BN due to catastrophic bubble formation between h-BN and $MoTe_2$ induced by an above-damage-threshold optical pulse. The methodology of "probe before destruction" has been demonstrated in various contexts including single-shot femtosecond X-ray nanocrystallography of radiation-sensitive biological systems[34-39]. In our case, the 800-nm pulse duration of 35 fs was faster than the onset of significant lattice motion in $MoTe_2$, which has been estimated[24,32] to be between 150 fs and 1 ps. The fidelity of this method was confirmed by measurements of SHG as a function of the optical polarization angle relative to the crystallographic axes. The results of single-shot measurements at high fluence were consistent with those at low fluence and with the 6-fold rotational symmetry expected for a hexagonal phase 2D crystal. (The details are shown in Supplementary Fig. S8.) The relatively large sizes and good uniformity of the trilayer crystals were sufficient to allow comparison for each flake among three locally destructive single-shot SHG measurements at different sample locations: one prior to THz excitation (initial signal intensity labeled I_i), a second at the selected delay time

following the THz excitation pulse ($I_{\Delta t}$), and a third at a long time (approximately 1 minute, final intensity I_f) after THz excitation. See **Figs. 3a and 3b**. The delay times Δt were -20 ps, 5 ps, 20 ps, 300 ps, 1.24 ns, 12.5 ns and 112.5 ns for different samples. The pump-probe experimental details can be found in Supplementary Note 3, Figs. S7, and S8.

Figure 3c shows that at long delay times after strong-field THz irradiation, the SHG signal from trilayer samples disappears as it does from monolayer and bilayer samples. Raman spectra of multilayer samples shown in Supplementary Fig. S16 confirm the disappearance of the 2H phase after irradiation of multilayer samples with a strong THz field, as in monolayer and bilayer samples. The gradual appearance of the 1T′ phase Raman peaks after further irradiation is far less evident in multilayer samples, but the disappearance of the 2H phase induced in a single THz shot may be similar among all the samples since even for monolayers there is little if any evidence of the 1T′ phase after one shot. Although the SHG signal disappears at long delay times Δt after the THz pulse, at short delay times we see complex kinetics. The SHG intensity increases initially, reaches a maximum of about twice its initial value I_i at 20 ps, remains higher than I_i for several hundred picoseconds and comparable to I_i for at least 1 ns, then drops to about $0.2I_i$ at Δt = 12.5 ns with no evidence of longer timescale dynamics. Similar short-time dynamical behavior was observed in bulk $MoTe_2$ flakes (> 10 layers) irradiated with THz field amplitude of 150 kV/cm, lower than the phase transition threshold. The results are shown in **Fig. 3d**. The observed nanosecond timescale for SHG reduction is comparable to the reported carrier recombination lifetimes[40] in few-layer $MoTe_2$. Images of the irradiated samples and experimental details appear in the Supplementary Fig. S9 and Note 4. The increase in SHG observed at shorter times requires further investigation. It may be associated with the first steps toward transformation into a metastable phase, perhaps the distorted trigonal prismatic phase labeled as $2H^*$ along the 2H-1T′ pathway[26,41]. The indefinite

persistence of a metastable phase after a single strong THz pulse or the 1T′ phase after further irradiation is likely due to the recombination of the THz-induced carriers after tens of nanoseconds, upon which the activation barriers rise again and prevent a return to the 2H phase.

The mechanisms of irreversible phase transition of monolayer $MoTe_2$ are studied by DFT calculations and understood in the framework of transition state theory. We first investigated the effect of charge (electron) doping on the energy landscape of phase transition as shown in **Fig. 4a**. In the neutral state, the metastable 1T′ phase is higher in energy than the 2H phase by about 0.1 eV. The activation barrier E_{act} and reverse activation barrier are found to be 1.66 eV and 1.56 eV respectively, which preserve the 2H and 1T′ phases in the presence of thermal fluctuations. We see a barrierless minor structural phase transition from 2H to $2H^*$ that can be triggered at small charge doping[41]. However, only upon adding charge carriers close to a density of 1 *e*/$MoTe_2$ unit, which corresponds to electron density at 9×10^{14} cm^{-2}, does the 1T′ phase become thermodynamically more stable than $2H^*$ phase as experimentally demonstrated in literature[6]. In our experiment, the density of excited electron-hole pairs is estimated to approach 10^{15} cm^{-2} through Poole-Frenkel tunneling and impact ionization, as discussed in Supplementary Note 1. However, the net charge doping effect should not be the dominant factors for the 1T′ phase in our experiment because only a low density of charges can be trapped at the defects sites in h-BN or h-BN/fused silica interfaces[41]. In order to provide a simple comparison with the experimental conditions, we approximate the highly non-equilibrium THz-excited carrier distribution by an equilibrium Fermi-Dirac distribution with a temperature smearing method. We used a smearing width up to 0.5 eV to have reasonable populations in the conduction band, corresponding to a carrier density of around 4×10^{14} cm^{-2}. We observe that the activation barrier E_{act} for 2H-to-1T′ transition can be lowered substantially with higher temperature smearing as shown in **Fig. 4b**,

which supports the notion that a THz-induced non-equilibrium carrier distribution is the primary reason for the 2H-1T′ phase transition. More discussion can be found in Supplementary Note 5 and Figs S10-S13.

We have demonstrated a THz-driven irreversible 2H to 1T′ phase transition in monolayer and bilayer $MoTe_2$. Single-shot SHG measurements following THz excitation indicate the timescale for the transformation out of the 2H phase to be within 10 ns. Our work shows that strong THz fields can be used to steer a quantum material among metastable and stable phases in complex multiphase landscapes and in some cases to switch into a phase that is long-lived or permanent. The prospects are particularly promising for THz control over the myriad quantum phases in 2D layered materials.

Methods

THz field enhancement metamaterial simulation and fabrication

The field of the free-space THz radiation can be enhanced with a metal microslit on a fused silica substrate as shown in **Fig. 1c**. Numerical simulations using commercial finite-difference time-domain (FDTD) software (FDTD solutions, Lumerical Inc) were performed to calculate the enhancement factor of the gold slits. The dielectric function of gold in the terahertz frequency range was approximated by a Drude model ($\varepsilon = \varepsilon_\infty - \omega_p^2/(\omega^2 + i\omega\gamma)$) with parameter values[42] from previous measurements (ε_∞ = 9.1, $\omega_p = 1.38\times10^{16}$ rad/s, $\gamma = 1.075\times10^{14}$ rad/s), and n = 1.96 was used for fused silica[43]. A light source was incident from the substrate side with an electric field along x direction. The source frequency spanned from 0.3 to 1.5 THz. Perfectly matched layers (PML) were used to absorb the scattered radiation in all directions. In the simulation, a power monitor was used to record the electric field along the gold surface.

The fabrication of the metal microslit array is based on a standard photolithography and lift-off process. Image reversal photoresist AZ5214 was spin-coated on a fused silica substrate at 3000 rpm for 30 s, soft baked at 110 °C for 50 s on a hotplate, UV exposed by a maskless aligner MLA 150 with a dose of 24 mJ/cm^2, and post-exposure baked at 120 °C for 2 min followed by flood exposure and development in AZ422. A thin film of 2 nm Cr was deposited onto the substrate as an adhesion layer by thermal evaporation followed by a 98 nm thick Au thin film. The sample was soaked in acetone and PG remover for lift-off to complete fabrication of the field enhancement structure.

Layered $MoTe_2$ integration with field enhancement structure

The monolayer, few-layer $MoTe_2$ and layered h-BN were exfoliated on SiO_2/Si substrate with bulk $MoTe_2$ (from HQ graphene) or h-BN crystal. Monolayer and bilayer $MoTe_2$ were identified by optical contrast and Raman spectroscopy. The layered materials were picked up by the transfer slide, composed of a stack of glass, a polydimethylsiloxane (PDMS) film and a polycarbonate (PC) film, as described in ref[44]. The resulting stacks of top h-BN layer, $MoTe_2$ monolayer, and bottom h-BN layer were then placed on top of the Au gap with the help of a transfer setup under an optical microscope[30].

High field terahertz pulse generation

High field terahertz pulses were generated in a Mg:$LiNbO_3$ crystal by tilting the optical pulse front to achieve phase matching[45]. By using a three-parabolic-mirror terahertz imaging system, the image of the terahertz spot on the sample was close to its diffraction limit or around 500 μm in diameter. The incident THz pulse was measured in the time domain using electro-optic sampling with a 100 μm thick 110-oriented gallium phosphide crystal. When pumping with a 4 W laser from an amplified Ti:sapphire laser (repetition rate 1 kHz, central wavelength 800 nm, pulse duration

100 fs), the maximum electric field of the THz pulses reached 270 kV/cm at the focus with a spectrum centered at 0.5 THz as shown in Supplementary Fig. S14.

Raman spectroscopy

Raman spectroscopy was performed on samples before and after THz irradiation using a commercial Raman system (Horiba LabRAM) with a helium-neon laser (λ=632.8 nm). The laser beam was focused on the samples by a 100× objective with numerical aperture 0.9, resulting in a beam diameter of about 1 μm.

Second harmonic generation mapping

As shown in Supplementary Fig. S5, the SHG fundamental pulses are provided by a mode-locked Ti:sapphire oscillator at 800nm. The laser pulse duration was around 35 fs at 80 MHz repetition rate. The excitation pulse was linearly polarized by an achromatic polarizer (400-800nm) and the polarization of the incident laser pulses on the sample was controlled by an achromatic half-wave plate in a motorized rotational stage. SHG from the sample was collected by the same objective and transmitted through the same half-wave plate and polarizer, which ensured that the SHG components detected were parallel to the polarization of the fundamental field. A photomultiplier tube (Hamamatsu Photonics H10721) was used to analyze the SHG signal in fast mapping. The laser beam on the sample was scanned using 2-axis Galvo mirrors (Thorlabs, GVS412) to acquire *in-situ* SHG images upon successive single THz pulse irradiations.

Single-shot THz pump-SHG probe microscopy

The THz pump arm is combined with SHG pulses from second, synchronized 12W amplified Ti:sapphire laser (repetition rate 1 kHz, central wavelength 800 nm, pulse duration 35 fs). SHG light was focused to a near-diffraction-limited size (1 μm) and near-transform-limited duration (~35 fs) at the sample with a 50× objective. The SHG light was collected by the same objective

and detected by a PMT with a confocal microscope to selectively probe the area at the focus with single-optical-pulse irradiation. The power level of the SHG excitation pulse is well above the damage threshold of 2D $MoTe_2$, but the ultrafast nature of the pulse enabled us to obtain a reliable SHG signal before the sample was damaged and turned into a plasma. The temporal overlap of the counter-propagating THz field and SHG optical pulse was determined by THz field-induced second harmonic signal (TFISH) from a thin lithium niobate slab (30 μm). All of the optical measurements were conducted on a single-shot basis at an ambient condition (300 K, 1 atm). More details can be found in Supplementary note 3, Fig. S7 and S8.

Acknowledgments:

The authors acknowledge discussions and technical supports from Z.F. Ren, Y. Yoon, B. Pein, P.-C.Shen, A. Maznev, T. Mahony, F. Gao and Y. Chen. J.S. and K.A.N acknowledge support from the U.S. Department of Energy, Office of Basic Energy Sciences, under Award No. DE-SC0019126. Y.-Q.B and P.J.-H acknowledge support from Gordon and Betty Moore Foundation's EPiQS Initiative through grant GBMF4541. W.C., S.F., and E.K. acknowledge support by ARO MURI award W911NF-14-0247 and STC Center for Integrated Quantum Materials, NSF Grant No. DMR-1231319. J.C.H and V.B. acknowledge support from the Center for Energy Efficient Electronics Science (NSF Award 0939514). Y.-Q.B and Z.C.L. acknowledge support from Hundred Talents Plan of Sun Yat-sen University 76120-18831112, 76120-18831111, NSFC61974167, the Science and Technology Department of Guangdong Province, and the Fundamental Research Funds for the Central Universities.

Author contributions:

Y.-Q.B and J.S. conceived and directed the research. J.S and Y.-Q.B performed all the experiments and analyzed the data under guidance from P.J.-H and K.A.N. W.C., S.F., and E.K. provided theoretical calculations. Y.-Q.B, J.C.H and V.B. synthesized field enhancement structures. Z.L.C performed the field enhancement calculations. T.T. and K.W. grew the crystals of hexagonal boron nitride. All authors wrote the manuscript together.

Additional information:

Supplementary information is available in the online version of the paper. Correspondence and requests for materials should be addressed to K.A.N, P.J.-H. and Y.-Q.B.

Competing financial interests:

The authors declare no competing financial interests.

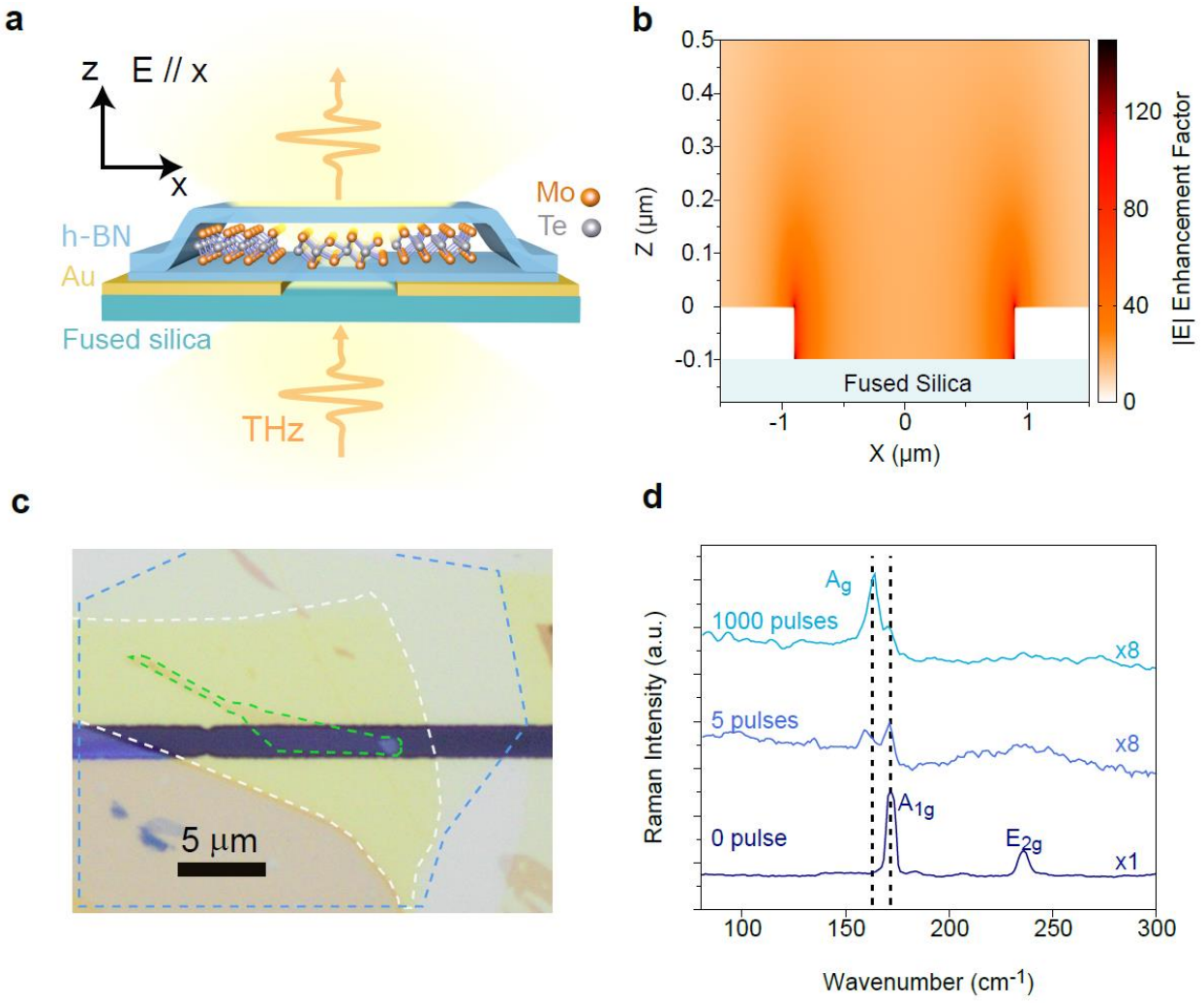

Figure 1 THz-driven irreversible phase transition in monolayer $MoTe_2$. a, Cross-sectional schematic illustration of a $MoTe_2$ crystal spanning an insulating gap between deposited gold lines, which serves as a THz field enhancement structure. The monolayer 2H-phase $MoTe_2$ crystal is encapsulated with top and bottom h-BN. THz pulses are incident from the fused silica substrate side. **b,** Numerical simulation results showing THz field enhancement by a factor of 20-50 in significant regions in and near the gap between gold lines (up to 120 maximum enhancement, but in regions too small to contribute significantly to our measurements). **c,** Optical image of a $MoTe_2$ sample, including 15 nm thick top h-BN (marked by a white dashed line), monolayer $MoTe_2$ (green dashed line), and 5 nm thick bottom h-BN (blue dashed line) all spanning a 1.8-μm gap (dark horizontal line) between gold strips. **d**, Raman spectra of monolayer $MoTe_2$ after successive THz pulse irradiation with free-space field amplitudes of 270 kV/cm. The A_g mode at 163.5 cm^{-1}, characteristic of 1T′ $MoTe_2$, appears clearly after 5 THz pulses and grows in further upon further irradiation, while the A_{1g} and E_{2g} modes of 2H-$MoTe_2$ at 171.5 cm^{-1} and 236 cm^{-1} are strongly reduced. The Raman measurements were conducted with a 1 μm diameter laser spot so they averaged over regions in the gap with varying enhanced THz field strengths.

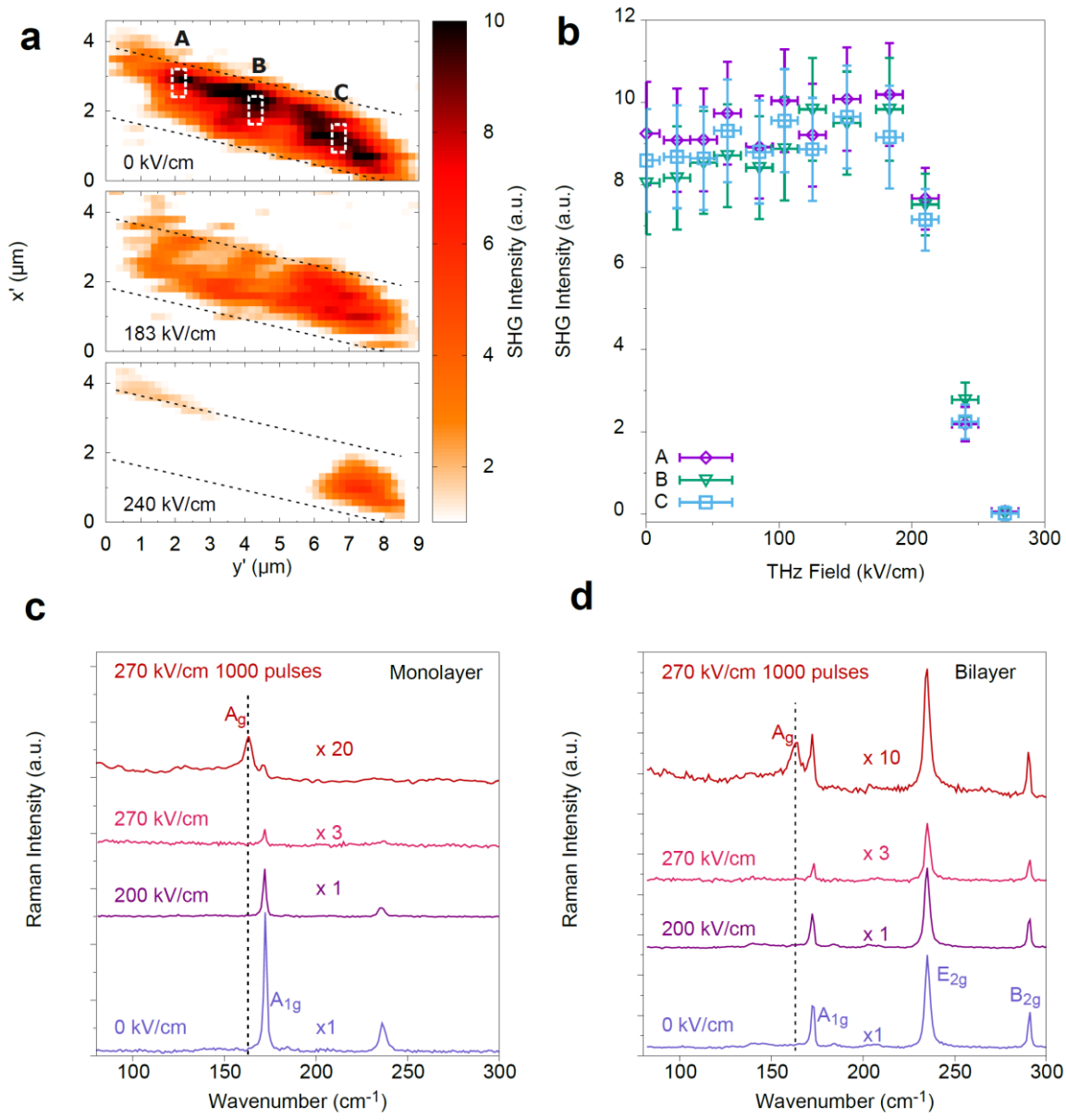

Figure 2 THz field dependence of the phase transition in monolayer and bilayer $MoTe_2$. a, SHG images of monolayer $MoTe_2$ before THz irradiation (0 kV/cm), after irradiation with one THz pulse at 183 kV/cm field amplitude, and after irradiation with a second THz pulse at 240 kV/cm. The dashed lines indicate the edges of gold layers in the field enhancement structure. Different areas of monolayer $MoTe_2$ in the gap are labeled A, B and C. **b**, SHG from different spots (A-C) in Fig. 2a measured after irradiation of the sample by single THz pulses with successively increasing field strength. The SHG signal begins to decrease at a free-space field strength of 200 kV/cm and completely disappears above 240 kV/cm. **c, d,** Raman spectra of monolayer and bilayer $MoTe_2$ samples prior to THz irradiation, after THz irradiation with a single pulse at 200 kV/cm, another single pulse at 270 kV/cm, and 1000 pulses at 270 kV/cm. The Raman modes of the 2H phase, including A_{1g}, E_{2g} and B_{2g} modes of the bilayer, start to decrease after a single THz pulse above 200 kV/cm. Both monolayer and bilayer samples show the A_g mode at 163.5 cm^{-1} after irradiation with 1000 pulses at 270 kV/cm.

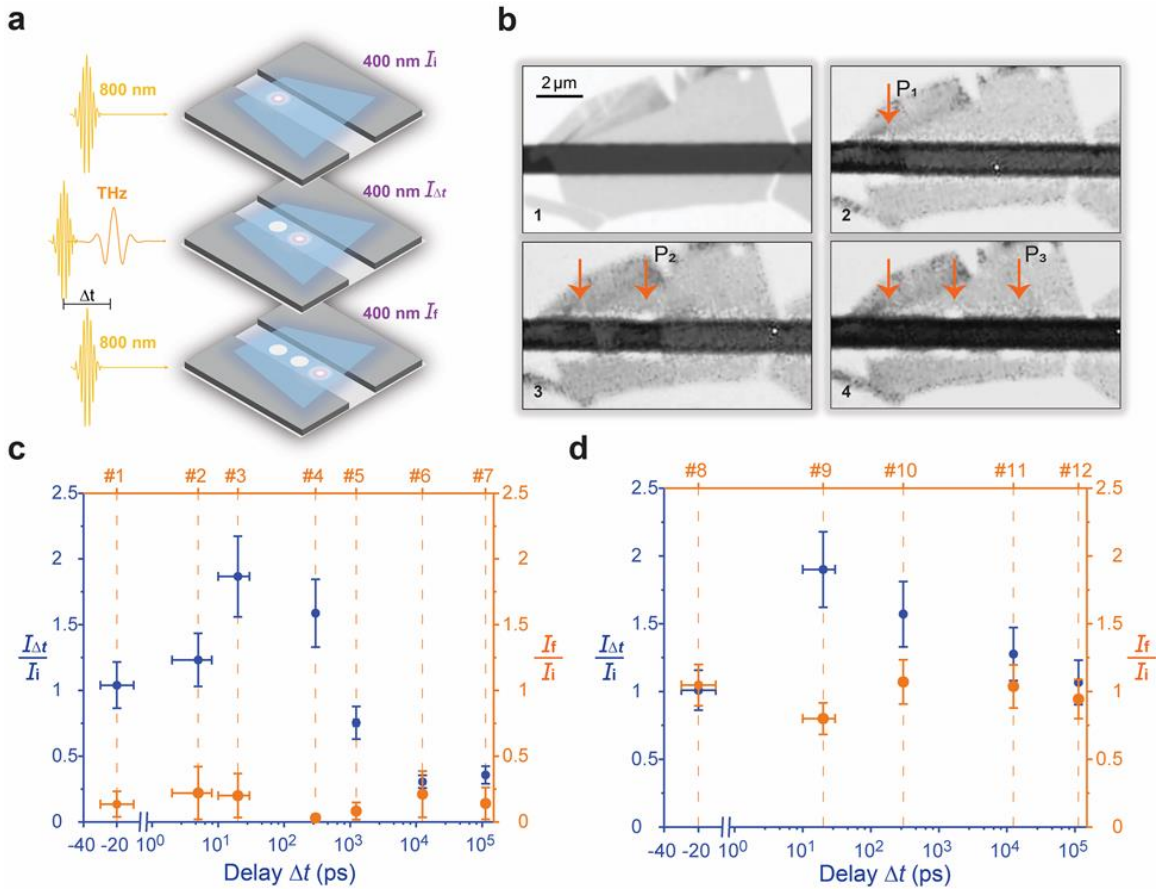

Figure 3 Single-shot SHG probe measurements were conducted to obtain the structural dynamics following a single THz excitation pulse. a, Schematic illustration of single-shot SHG probe before and after a THz excitation pulse. Single-shot measurements were conducted with 800-nm pulses at three sample locations to record the SHG intensity from the sample in its initial state prior to the THz pulse (I_i), at a specified delay time after the THz pulse ($I_{\Delta t}$), and in its final state ~ 1 minute after the THz pulse (I_f). The 35-fs, 800-nm probe pulses were focused to a spot size of ~ 1 μm in the center of the microslit gap, where the THz excitation fluence was about 20 mJ/cm^2. **b**, Optical images of a trilayer $MoTe_2$ sample used for SHG measurement. The pristine sample is shown in image 1 taken with a high resolution camera; images 2-4 were taken in-situ with a low resolution camera. Image 2 was taken after measurement of SHG signal I_i by the first 800 nm pulse P_1. Image 3 was taken after another SHG signal I_i was measured by a second 800 nm pulse P_2; Image 4 was taken after THz excitation with 270 kV/cm field strength and measurement of SHG signal $I_{\Delta t}$ by the third pulse P_3. The optically damaged regions are indicated by orange arrows. The reduced optical reflectivity of the sample is apparent after THz irradiation which permanently removed the initial 2H phase of $MoTe_2$. **c,** SHG intensities measured from seven trilayer $MoTe_2$ samples at different delay times Δt from several picoseconds to hundreds of nanoseconds (blue dots) as well as around 1 minute (yellow dots). The data points on the same line show the SHG signal intensities measured from the same sample shortly after and long after the THz excitation pulse, normalized by the SHG signal intensity prior to THz excitation. **d,** Similar single-shot pump-probe measurements on five bulk $MoTe_2$ flakes. The free-space THz field strength was 150 kV/cm which was below the irreversible phase transition threshold. The 20 mJ/cm^2 probe pulse fluence was above the optical damage threshold.

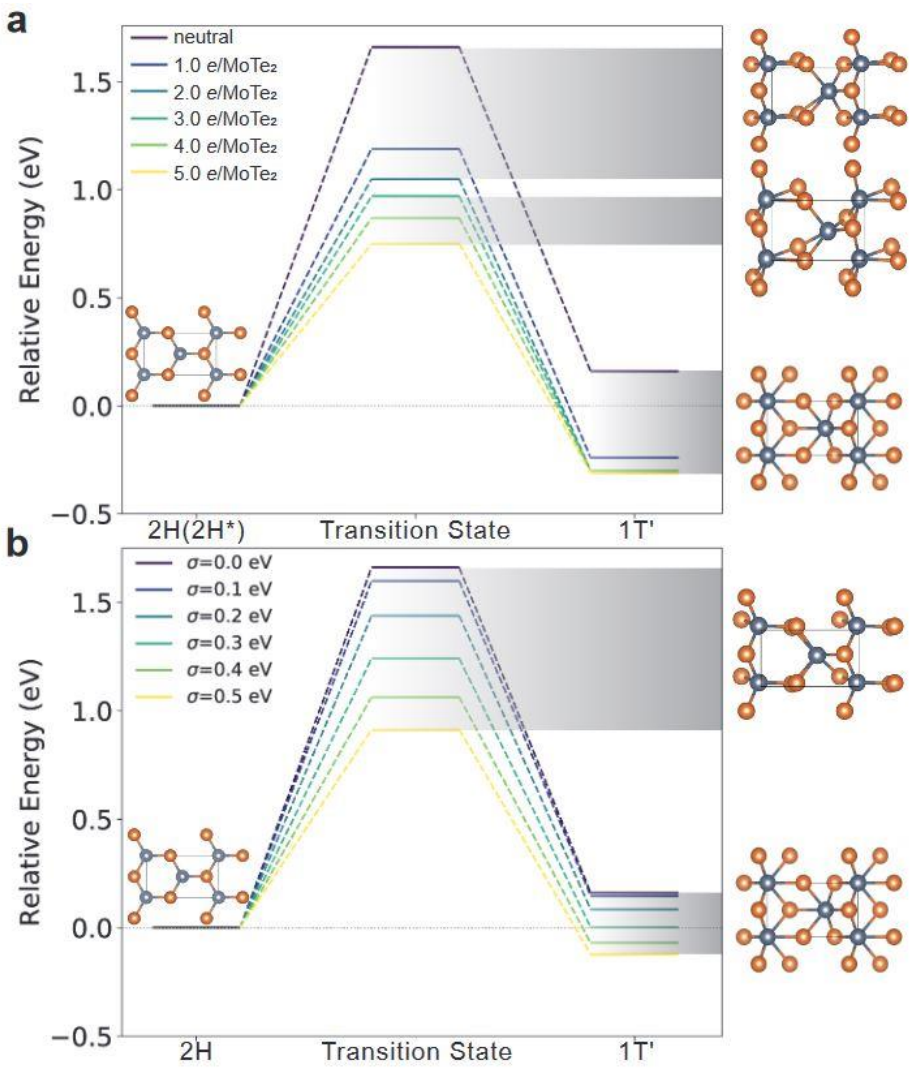

Figure 4 DFT-calculated energy landscape of phase transition with charge doping and carrier excitation. a, Energies of 2H phase at neutral state and 2H* phase at charged states are set at zero. As the added charge density increases to 1.0 *e*/$MoTe_2$, which corresponds to 9×10^{14} cm^{-2}, the activation energy decreases from 1.66 eV to 1.19 eV. Since the net charge density in the sample is estimated to be much lower than the charge density used in the 2H to 1T′ calculation, charge doping is not the main reason for formation of the 1T′ phase although it could trigger the 2H to 2H* phase transition according to the DFT calculation. **b**, Non-equilibrium distribution of carriers is qualitatively described by the Fermi-smearing method. The free-energy barrier decreases from 1.66 to 0.91 eV as the Fermi-smearing width increases from 0.0 to 0.5 eV. The atomic structures of 2H* and transition states are displayed in the Supplementary Figs. S10,11,12.

Reference

1 Liu, M. *et al.* Terahertz-field-induced insulator-to-metal transition in vanadium dioxide metamaterial. *Nature* 487, 345-348 (2012).

2 Dienst, A. *et al.* Optical excitation of Josephson plasma solitons in a cuprate superconductor. *Nature Materials* 12, 535 (2013).

3 Li, X. *et al.* Terahertz field–induced ferroelectricity in quantum paraelectric $SrTiO_3$. *Science* 364, 1079-1082 (2019).

4 Schlauderer, S. *et al.* Temporal and spectral fingerprints of ultrafast all-coherent spin switching. *Nature* 569, 383-387 (2019).

5 Manzeli, S., Ovchinnikov, D., Pasquier, D., Yazyev, O. V. & Kis, A. 2D transition metal dichalcogenides. *Nature Reviews Materials* 2, 17033 (2017).

6 Wang, Y. *et al.* Structural phase transition in monolayer $MoTe_2$ driven by electrostatic doping. *Nature* 550, 487 (2017).

7 Qian, X., Liu, J., Fu, L. & Li, J. Quantum spin Hall effect in two-dimensional transition metal dichalcogenides. *Science* 346, 1344-1347 (2014).

8 Chen, X., Gu, Z.-C. & Wen, X.-G. Local unitary transformation, long-range quantum entanglement, wave function renormalization, and topological order. *Physical Review B* 82, 155138 (2010).

9 Basov, D. N., Averitt, R. D. & Hsieh, D. Towards properties on demand in quantum materials. *Nature Materials* 16, 1077 (2017).

10 Xu, Y. *et al.* Observation of topological surface state quantum Hall effect in an intrinsic three-dimensional topological insulator. *Nature Physics* 10, 956 (2014).

11 Conan, A., Bonnet, A., Amrouche, A. & Spiesser, M. Semiconducting properties and band structure of $MoTe_2$ single crystals. *Journal de Physique* 45, 459-465 (1984).

12 Achintya, B., Anjali, S., Muthu, D. V. S., Waghmare, U. V. & Sood, A. K. Pressure-dependent semiconductor to semimetal and Lifshitz transitions in 2H-$MoTe_2$: Raman and first-principles studies. *Journal of Physics: Condensed Matter* 29, 105403 (2017).

13 Zhou, Y. *et al.* Pressure-induced Td to 1T' structural phase transition in WTe_2. *AIP Advances* 6, 075008 (2016).

14 Yu, Y. *et al.* Gate-tunable phase transitions in thin flakes of 1T-TaS_2. *Nature Nanotechnology* 10, 270 (2015).

15 Kappera, R. *et al.* Phase-engineered low-resistance contacts for ultrathin MoS_2 transistors. *Nature Materials* 13, 1128 (2014).

16 Zhu, J. *et al.* Argon plasma induced phase transition in monolayer MoS_2. *Journal of the American Chemical Society* 139, 10216-10219 (2017).

17 Stojchevska, L. *et al.* Ultrafast switching to a stable hidden quantum state in an electronic crystal. *Science* 344, 177-180 (2014).

18 Keum, D. H. *et al.* Bandgap opening in few-layered monoclinic $MoTe_2$. *Nature Physics* 11, 482 (2015).

19 Cho, S. *et al.* Phase patterning for ohmic homojunction contact in $MoTe_2$. *Science* 349, 625 (2015).

20 Zhou, L. *et al.* Synthesis of high-quality large-area homogenous 1T' $MoTe_2$ from chemical vapor deposition. *Advanced Materials* 28, 9526-9531 (2016).

21 Chen, S.-Y., Naylor, C. H., Goldstein, T., Johnson, A. T. C. & Yan, J. Intrinsic phonon bands in high-quality monolayer T' Molybdenum Ditelluride. *ACS Nano* 11, 814-820 (2017).

22 Fan, K. *et al.* Nonlinear Terahertz metamaterials via field-enhanced carrier dynamics in GaAs. *Physical Review Letters* 110, 217404 (2013).

23 Gray, A. X. *et al.* Ultrafast terahertz field control of electronic and structural interactions in vanadium dioxide. *Physical Review B* 98, 045104 (2018).

24 Bo Peng, H. Z., Weiwen Chen, Zhi-Jun Qiu, Hezhu Shao, Heyuan Zhu, Bartomeu Monserrat, Desheng Fu, Hongming Weng. Ultrafast Photo-induced Phase Transition in 2D $MoTe_2$. *ArXiv:1903.09757* (2019).

25 Krishnamoorthy, A. *et al.* Semiconductor–metal structural phase transformation in $MoTe_2$ monolayers by electronic excitation. *Nanoscale* 10, 2742-2747 (2018).
26 Kolobov, A. V., Fons, P. & Tominaga, J. Electronic excitation-induced semiconductor-to-metal transition in monolayer $MoTe_2$. *Physical Review B* 94, 094114 (2016).
27 Yeh, K. L., Hoffmann, M. C., Hebling, J. & Nelson, K. A. Generation of 10μJ ultrashort terahertz pulses by optical rectification. *Applied Physics Letters* 90, 171121 (2007).
28 Pein, B. *et al.* Terahertz-driven luminescence and colossal stark effect in CdSe:CdS colloidal quantum dots. *Nano Letters* 17, 5375-5380 (2017).
29 Wang, L. *et al.* One-Dimensional Electrical Contact to a Two-Dimensional Material. *Science* 342, 614-617 (2013).
30 Dean, C. R. *et al.* Boron nitride substrates for high-quality graphene electronics. *Nature Nanotechnology* 5, 722 (2010).
31 Ruppert, C., Aslan, O. B. & Heinz, T. F. Optical properties and band gap of single- and few-Layer $MoTe_2$ crystals. *Nano Letters* 14, 6231-6236 (2014).
32 Froehlicher, G. *et al.* Unified description of the optical phonon modes in N-layer $MoTe_2$. *Nano Letters* 15, 6481-6489 (2015).
33 Song, Y. *et al.* Second Harmonic Generation in Atomically Thin $MoTe_2$. *Advanced Optical Materials* 6, 1701334 (2018).
34 Chapman, H. N. *et al.* Femtosecond X-ray protein nanocrystallography. *Nature* 470, 73 (2011).
35 Seibert, M. M. *et al.* Single mimivirus particles intercepted and imaged with an X-ray laser. *Nature* 470, 78 (2011).
36 Boutet, S. *et al.* High-resolution protein structure determination by serial femtosecond crystallography. *Science* 337, 362-364 (2012).
37 Redecke, L. *et al.* Natively inhibited Trypanosoma brucei Cathepsin B structure determined by using an X-ray laser. *Science* 339, 227-230 (2012).
38 Aquila, A. *et al.* Time-resolved protein nanocrystallography using an X-ray free-electron laser. *Optics Express* 20, 2706-2716 (2012).
39 Tenboer, J. *et al.* Time-resolved serial crystallography captures high-resolution intermediates of photoactive yellow protein. *Science* 346, 1242-1246 (2014).
40 Chen, K. *et al.* Accelerated carrier recombination by grain boundary/edge defects in MBE grown transition metal dichalcogenides. *APL Materials* 6, 056103 (2018).
41 Zhang, F. *et al.* Electric-field induced structural transition in vertical $MoTe_2$- and $Mo_{1-x}W_xTe_2$-based resistive memories. *Nature Materials* 18, 55-61 (2019).
42 Johnson, P. B. & Christy, R. W. Optical constants of the noble metals. *Physical Review B* 6, 4370-4379 (1972).
43 Naftaly, M. & Miles, R. E. Terahertz time-domain spectroscopy for material characterization. *Proceedings of the IEEE* 95, 1658-1665 (2007).
44 Zomer, P. J., Guimarães, M. H. D., Brant, J. C., Tombros, N. & van Wees, B. J. Fast pick up technique for high quality heterostructures of bilayer graphene and hexagonal boron nitride. *Applied Physics Letters* 105, 013101 (2014).
45 Hebling, J., Yeh, K.-L., Hoffmann, M. C., Bartal, B. & Nelson, K. A. Generation of high-power terahertz pulses by tilted-pulse-front excitation and their application possibilities. *J. Opt. Soc. Am. B* 25, B6-B19 (2008).